
The role of hydrogen incorporation into amorphous carbon films in the change of the secondary electron yield

[Nenad Bundaleski](#)^{*}, [Carolina F Adame](#), Eduardo Alves, Nuno P Barradas, Maria F Cerqueira, [Jonas Deuermeier](#), Yorick Delaup, [Ana M Ferraria](#), [Isabel Ferreira](#), Holger Neupert, Marcel Himmerlich, Ana Maria M.B. do Rego, Martino Rimoldi, Orlando M.N.D. Teodoro, [Mikhail I. Vasilevskiy](#), Pedro Costa Pinto

Posted Date: 19 July 2023

doi: 10.20944/preprints202307.1315.v1

Keywords: amorphous Carbon, particle accelerators, SEY, XPS, Raman spectroscopy.



Preprints.org is a free multidiscipline platform providing preprint service that is dedicated to making early versions of research outputs permanently available and citable. Preprints posted at Preprints.org appear in Web of Science, Crossref, Google Scholar, Scilit, Europe PMC.

Copyright: This is an open access article distributed under the Creative Commons Attribution License which permits unrestricted use, distribution, and reproduction in any medium, provided the original work is properly cited.

Article

The Role of Hydrogen Incorporation into Amorphous Carbon Films in the Change of the Secondary Electron Yield

Nenad Bundaleski^{1*}, Carolina F. Adame¹, Eduardo Alves^{2,3}, Nuno P. Barradas^{2,3}, Maria F. Cerqueira^{4,5}, Jonas Deuermeier⁶, Yorick Delaup⁹, Ana M. Ferraria^{7,8}, I.M.M. Ferreira⁶, Holger Neupert⁹, Marcel Himmerlich⁹, Ana Maria M.B. do Rego^{7,8}, Martino Rimoldi⁹, Orlando M.N.D. Teodoro¹, Mikhail Vasilevskiy^{4,5} and Pedro Costa Pinto^{9*}

¹ CEFITEC, Departamento de Física, Faculdade de Ciências e Tecnologia, Universidade Nova de Lisboa, Campus de Caparica, 2829-516 Caparica, Portugal

² DECN, Instituto Superior Técnico, University of Lisbon, Bobadela 2695-066, Portugal

³ IPFN, Instituto Superior Técnico, University of Lisbon, Lisbon 1049-001, Portugal

⁴ Centre of Physics of the Universities of Minho and Porto (CF-UM-UP) & Laboratório de Física para Materiais e Tecnologias Emergentes (LaPMET), Braga, 4710-057, Portugal

⁵ International Iberian Nanotechnology Laboratory (INL), Av. Mestre José Veiga, 4715-330 Braga, Portugal

⁶ i3N/CENIMAT, Departamento de Ciência dos Materiais, Faculdade de Ciências e Tecnologia, Universidade Nova de Lisboa, Campus de Caparica, 2829-516 Caparica, Portugal

⁷ iBB—Institute for Bioengineering and Biosciences and Departamento de Engenharia Química, Instituto Superior Técnico, Universidade de Lisboa, Av. Rovisco Pais, 1049-001 Lisbon, Portugal

⁸ Associate Laboratory i4HB—Institute for Health and Bioeconomy at Instituto Superior Técnico, Universidade de Lisboa, Av. Rovisco Pais, 1049-001 Lisbon, Portugal.

⁹ European Organization for Nuclear Research, CERN, 1211 Geneva 23, Switzerland

* Correspondence: Pedro.Costa.Pinto@cern.ch; Tel.: +41 754 114 468; PCP; n.bundaleski@fct.unl.pt; Tel.: +351 920 552 850; NB

Abstract: The interest on amorphous carbon thin films with low secondary electron yield (SEY) has been increasing in the last years, to mitigate electron multipacting in particle accelerators and in RF devices. Previous works found that the SEY increases with the hydrogen amount and correlates with the Tauc gap. In this work, we analyse films produced by magnetron sputtering with different contents of hydrogen and deuterium, incorporated via target poisoning and sputtering of C₂D₂ molecules. XPS was implemented to estimate the phase composition of the films. The maximal SEY was found to decrease linearly with the fraction of the graphitic phase in the films. These results are supported by Raman scattering and UPS. The graphitic phase decreases almost linearly for hydrogen and deuterium concentrations between 12% and 46% (at.), but abruptly decreases when the concentration reaches 53%. This vanishing of the graphitic phase is accompanied by a strong increase of SEY and of the Tauc gap. These results suggest that the SEY is not dictated directly by the concentration of H/D but by the fraction of graphitic phase. The results are supported by a model used to calculate SEY of films consisting of a mixture of graphitic and polymeric phases.

Keywords: amorphous carbon; particle accelerators; SEY; XPS; Raman spectroscopy

1. Introduction

The emission of secondary electrons from surfaces plays a key role on the generation of electron multipacting in high power radio frequency devices and particle accelerators with positively charged beams. In particle accelerators, it can result in the formation of clouds of electrons, causing beam instabilities, deterioration of the vacuum, or heat loads to cryogenics parts of the system, limiting the overall efficiency of the accelerator (i.e. the beam luminosity) [O. Gröbner, Bunch induced multipactoring, CM-P0064850, CERN Libraries, Geneva, Switzerland, presented at the 10th International Conference on High-Energy Accelerators, 11th-17th of July 1977, Serpukhov, USSR—G. Skripka, G. Iadarola, L. Mether, G. Rumolo, Non-monotonic dependence of heat loads induced by electron cloud on bunch population at the LHC, Eur. Phys. J. Plus 137 (2022) 849]. A possible cure to this problem is to reduce the electron emission by coating the

internal surfaces of the vacuum chambers with a thin film of low Secondary Electron Yield (SEY) material. Amorphous carbon (a-C) coatings have been successfully used in the Super Proton Synchrotron at CERN (European Organisation for Nuclear Research) to mitigate the electron multipacting [C. Yin Vallgren, G. Arduini, J. Bauche, S. Calatroni, P. Chiggiato, K. Cornelis, P. Costa Pinto, B. Henrist, E. Métral, H. Neupert, G. Rumolo, E. Shaposhnikova, M. Taborelli, Amorphous carbon coatings for the mitigation of electron cloud in the CERN super proton synchrotron, *Phys. Rev. ST Accel. Beams* 14 (2011) 071001], and it is now in the baseline for the High Luminosity upgrade of the Large Hadron Collider, (CERN, Switzerland), and the Electron Ion Collider, (Brookhaven National Laboratory, USA) [F. Willeke, J. Beebe-Wang, Electron Ion Collider Conceptual Design Report 2021. United States: N. p., 2021. Web. doi:10.2172/1765663, S. Verdú-Andrés et al., A beam screen to prepare the RHIC vacuum chamber for EIC hadron beams: conceptual design and requirements, 12th International Particle Accelerator Conference - IPAC'21, May 24 - 28, 2021 Web. <https://www.osti.gov/servlets/purl/1784486>].

Secondary electron emission can be conveniently described as follows [R.F. Egerton, *Electron-Energy Loss Spectroscopy in the Electron Microscope* 3rd edn. Springer, New York, 2011]. Primary electrons that penetrate a material mainly lose their energy by different types of electron excitations (via plasmon excitations or by a direct energy transfer to valence and core electrons). This results in the generation of secondary electrons inside the material, with energy above the vacuum level. On their way out, these internal secondary electrons can efficiently lose their energy only by excitation of valence electrons. Finally, once they reach the surface, only the internal secondary electrons which still have energy above the vacuum level have a chance to be emitted. The whole process is strongly affected by the electronic structure of the material, which determines the energy loss processes of both primary and internal secondary electrons. Particularly important is the latter, which can be reduced by opening the energy gap. This is the origin of the high SEY of dielectric materials [S. Ono, K. Kanaya, The energy dependence of secondary emission based on the range-energy retardation power formula, *J. Phys. D: Appl. Phys.* 12 (1979) 619].

The efficiency of a-C coatings for suppressing electron multipacting depends on structural properties: only coatings with pronounced electrical conductivity can have a low SEY. It has been well established that the presence of hydrogen impurities is particularly harmful in that respect [P. Costa Pinto, et al., Carbon coating of the SPS dipole chambers. *AIP Conf. Proc.* C 12 (August 2013) 141–148, A. Santos, N. Bundaleski, B.J. Shaw, A.G. Silva, O.M.N.D. Teodoro, Increase of Secondary Electron Yield of Amorphous Carbon Coatings under High Vacuum Conditions. *Vacuum* 98 (2013) 37-40]. The effects of hydrogen and nitrogen impurities on the secondary electron emission properties of a-C coatings were a subject of two recent studies [H. M. Fernández, M. Himmerlich, P. Costa Pinto, J. Coroa, D. Sousa, A. Baris, M. Taborelli, The impact of H₂ and N₂ on the material properties and secondary electron yield of sputtered amorphous carbon films for anti-multipacting applications, *Appl. Surf. Sci.* 542 (2021) 148552, C.F. Adame, E. Alves, N.P. Barradas, P. Costa Pinto, Y. Delaup, I.M.M. Ferreira, H. Neupert, M. Himmerlich, S. Pfeiffer, M. Rimoldi, M. Taborelli, O.M.N.D. Teodoro, N. Bundaleski, Amorphous carbon thin films: mechanisms of hydrogen incorporation during magnetron sputtering and consequences for the secondary electron emission, *J. Vac. Sci. Technol. A* 41 (2023) 043412]. It was clearly demonstrated that adding hydrogen or deuterium in the discharge gas increases the SEY of carbon films, while the presence of nitrogen has an opposite effect. By combining SEY measurements with Ion Beam Analysis (IBA), a correlation between the deuterium content and the maximum SEY (SEY_{max}) was established. SEY_{max} increases linearly, from 1 to 1.4, with the overall hydrogen and deuterium (H + D) relative content up to 47%. Further increase of the H + D amount up to 54% is accompanied by a steep SEY_{max} growth to 2.2. The samples were also investigated by Optical Absorption Spectroscopy (OAS), enabling estimation of the optical energy gap using the procedure established by Tauc (so-called Tauc gap). These results reveal a strong correlation between the SEY_{max} and the Tauc gap, apparently offering a straightforward explanation for the SEY_{max} increase. However, a-C films are often non-uniform, i.e., they may consist of various regions with different composition and electronic structure (e.g., graphitic, diamond-like and hydrocarbon domains, the latter being a result of highly common hydrogen contamination) [A.C. Ferrari, J. Robertson, Interpretation of Raman spectra of disordered and amorphous carbon, *Phys. Rev. B* 61 (2000) 14095]. Such materials have different local energy gaps, limiting the interpretation of Tauc plots [D. Roy, G. F. Samub, M. K. Hossain, C. Janáky, K. Rajeshwar, On the measured optical bandgap values of inorganic oxide semiconductors for solar fuels generation, *Catalysis Today* 300 (2018) 136-144].

Robertson summarized measurements of the Tauc gap performed on different types of a-C (pure and hydrogenated) in his seminal review paper [J. Robertson, Diamond-like amorphous carbon, *Mat. Sci.*

& Engineering R 37 (2002) 129-281]. He concluded that the Tauc gap of a film is not determined by the hydrogen content, but by the relative amount and properties of the sp^2 carbon phase. Local energy gaps of diamond-like and various hydrocarbon phases are too large to be related with a Tauc gap below ≈ 2 eV. The gap is therefore related to the configuration of π states on the sp^2 sites. In a planar cluster model, the band gap of a given cluster is inversely proportional to the square root of the number of the hexagonal rings in the cluster [A.C. Ferrari, J. Robertson, Interpretation of Raman spectra of disordered and amorphous carbon, Phys. Rev. B, 61 (2000) 14095]. Different types of defects (e.g., formation of pentagons or heptagons) will also open the gap. From this perspective, deviation from the linear dependence at low photon energies in Tauc plots should not be attributed to the so-called tail states (i.e., Urbach tail) but to the small quantity of graphitic clusters with small local energy gaps.

The abrupt increase of SEY_{max} , when the H+D relative concentration changes from 47% to 54%, suggests that the hydrogen content may not be directly responsible for the change of the secondary electron emission (SEE) properties of a-C. This doubt is further supported by the high correlation between the SEY_{max} and the Tauc gap [H. M. Fernández, M. Himmerlich, P. Costa Pinto, J. Coroa, D. Sousa, A. Baris, M. Taborelli, The impact of H₂ and N₂ on the material properties and secondary electron yield of sputtered amorphous carbon films for anti-multipacting applications, Appl. Surf. Sci. 542 (2021) 148552, C.F. Adame, E. Alves, N.P. Barradas, P. Costa Pinto, Y. Delaup, I.M.M. Ferreira, H. Neupert, M. Himmerlich, S. Pfeiffer, M. Rimoldi, M. Taborelli, O.M.N.D. Teodoro, N. Bundaleski, Amorphous carbon thin films: mechanisms of hydrogen incorporation during magnetron sputtering and consequences for the secondary electron emission, J. Vac. Sci. Technol. A 41 (2023) 043412], knowing that the Tauc gap can be independent of the hydrogen concentration [J. Robertson, Diamond-like amorphous carbon, Mat. Sci. & Engineering R 37 (2002) 129-281]. This aspect motivates our study: since the Tauc gap in a-C is known to be affected by the concentration and size of graphitic domains, could the latter also influence the SEE?

In our recent work we performed deposition of a-C coatings using magnetron sputtering in Ar discharges with several fractions of D₂, identified the mechanism behind the incorporation of deuterium in the films during the production phase and its impact on the SEY [C.F. Adame, E. Alves, N.P. Barradas, P. Costa Pinto, Y. Delaup, I.M.M. Ferreira, H. Neupert, M. Himmerlich, S. Pfeiffer, M. Rimoldi, M. Taborelli, O.M.N.D. Teodoro, N. Bundaleski, Amorphous carbon thin films: mechanisms of hydrogen incorporation during magnetron sputtering and consequences for the secondary electron emission, J. Vac. Sci. Technol. A 41 (2023) 043412]. In this work we report detailed analysis of the same samples by means of different electron and vibrational spectroscopic techniques. X-ray and UV Photoelectron Spectroscopies (XPS and UPS, respectively) were used to determine the surface composition, to identify different phases in the a-C films, and obtain information on their electronic structure. Further insights are provided by Raman scattering, Fourier Transform Infrared Spectroscopy (FTIR) and High Resolution Electron Energy Loss Spectroscopy (HREELS). Raman scattering, enabling the detection of the presence of graphitic carbon, was particularly valuable in supporting the XPS results. FTIR and HREELS were used to identify the character of C-D bonds in the most contaminated samples. These results are then compared with the corresponding SEY, OAS and IBA measurements, enabling us to reveal the actual mechanism behind the SEY increase by the hydrogen contamination.

2. Materials and Methods

All details of the thin film deposition procedure are explained in [C.F. Adame, E. Alves, N.P. Barradas, P. Costa Pinto, Y. Delaup, I.M.M. Ferreira, H. Neupert, M. Himmerlich, S. Pfeiffer, M. Rimoldi, M. Taborelli, O.M.N.D. Teodoro, N. Bundaleski, Amorphous carbon thin films: mechanisms of hydrogen incorporation during magnetron sputtering and consequences for the secondary electron emission, J. Vac. Sci. Technol. A 41 (2023) 043412]. Briefly, the films were deposited by magnetron sputtering from a 50 mm diameter graphite target. The total operating pressure was set to 2 Pa, consisting of Ar and small quantities of D₂, to study deuterium incorporation into the films. The substrates were mounted 93 mm away from the graphite target and the discharge power fixed at 30 W. Five sets of samples were deposited on Si single crystal and quartz substrates for different characterisations: the reference (without D₂ added to the discharge gas), 0.2D (0.2 vol% of added D₂), 0.5D (0.5 vol% of D₂), 1D (1.3 vol% of D₂) and 10D (10.9 vol% of D₂). D₂ was added to distinguish deliberately introduced contaminants from hydrogen contamination from the residual gas. The system was baked prior to each run for 24 h at 230 °C to minimize the natural contamination, keeping the residual gas pressure in the low 10⁻⁶ Pa range or better (N₂ equivalent). A new graphite target was used for each run. The deposition rate was 10-15 nm/h, generally growing with the D₂ partial pressure, pD_2 . The thin film

thicknesses are in the range from 486–719 nm (measured by SEM). The samples were transferred to different laboratories in stainless steel vacuum chambers, pre-evacuated by a turbomolecular pump and filled with N₂ gas.

UPS and XPS measurements of 'as-received' samples were performed on AXIS SUPRA setup (Kratos Analytical), containing both UPS and monochromatic XPS sources. XPS measurements were performed using the monochromatic Al K α line (photon energy of 1486.7 eV), and the spectrometer pass energy of 80 eV (survey spectra) and 5 eV (high resolution spectra). UPS measurements were performed by means of the He I α line (photon energy of 21.22 eV) and the spectrometer pass energy of 5 eV. The binding energy scale for UPS and XPS measurements were both calibrated using a sputter-cleaned Ag sample, based on the position of the Ag 3d_{5/2} line and of the top of the valence band. Fitting of graphitic contributions was based on the XPS measurements of freshly cleaved Highly Oriented Pyrolytic Graphite (HOPG). A correction of the raw UPS spectra was made by removing the contributions of the He I β line (energy shift of 1.87 eV, intensity of 1.2% with respect to the He I α line). All samples were conductive, apart from the sample 10D, which was measured with charge compensation using an electron flood gun.

Raman spectroscopy measurements were carried out at room temperature in a backscattering geometry on an alpha 300 R confocal Raman microscope (WITec) using a 532 nm Nd:YAG laser (2nd harmonic) as well as a 633 nm He-Ne laser for excitation. The laser beam with a power of 0.7 mW was focused on the sample by a $\times 50$ lens (Zeiss), providing a spot with a diameter of about 1 μ m. The spectra were collected with a 600 groove/mm grating using 5 acquisitions with a 2 s acquisition time. The same setup was used to perform photoluminescence measurements with two excitation wavelengths, 532 nm and 633 nm. For each sample, the spectra were acquired on several spots to check their lateral uniformity.

FTIR measurements were performed in vacuum in the wave number range 500–5000 cm⁻¹, using a Vertex 80v system (Bruker) in conventional reflection and transmission mode, as well as in the attenuated total reflection (ATR) configuration using a Ge crystal.

HREELS measurements were performed in a UHV system (operating pressure in the 10⁻⁷ Pa range) using a LK Technologies 2000R spectrometer. Further details on this experimental setup are provided in the Appendix A, together with the experimental results.

3. Results

3.1. Composition, Electron Emission and Optical Properties of the Coatings

In this section, we summarise the main results of the thin films obtained by different techniques and reported in [C.F. Adame, E. Alves, N.P. Barradas, P. Costa Pinto, Y. Delaup, I.M.M. Ferreira, H. Neupert, M. Himmerlich, S. Pfeiffer, M. Rimoldi, M. Taborelli, O.M.N.D. Teodoro, N. Bundaleski, Amorphous carbon thin films: mechanisms of hydrogen incorporation during magnetron sputtering and consequences for the secondary electron emission, *J. Vac. Sci. Technol. A* 41 (2023) 043412]. Thin film composition analysis performed by IBA revealed the presence of C, D, H and O uniformly distributed along the film depth, as confirmed by Secondary Ion Mass Spectrometry measurements. Results of the quantitative composition, the mass densities of the films, estimated from the IBA measurements and the film thicknesses (obtained by Scanning Electron Microscopy), as well as the results of SEY and Tauc gap (E_T) measurements are summarised in Table 1. The amount of incorporated deuterium steadily increases with D₂ partial pressure in the discharge gas (p_{D_2}), getting relatively close to the theoretical maximum of 65 at.%, corresponding to saturated hydrocarbons. The dependence of the maximum secondary electron yield (SEY_{max}) on p_{D_2} in the films has a distinctively different trend: an increase of the H/D amount from 10 to 46 at.% changes SEY_{max} from 0.99 to 1.38, while additional 7 at.% of H/D increases the SEY_{max} abruptly to 2.2. SEY_{max} and the Tauc gap are strongly correlated. It appears that small changes of the D/H content in samples 1D and 10D are accompanied by the very different electronic structures, which govern both the secondary electron emission and optical properties. The latter is also clear from the fact that the sample 1D was conductive in contrast to the sample 10D. Namely the latter motivated usage of different approaches for the SEY measurements of the two samples [C.F. Adame, E. Alves, N.P. Barradas, P. Costa Pinto, Y. Delaup, I.M.M. Ferreira, H. Neupert, M. Himmerlich, S. Pfeiffer, M. Rimoldi, M. Taborelli, O.M.N.D. Teodoro, N. Bundaleski, Amorphous carbon thin films: mechanisms of hydrogen incorporation during magnetron sputtering and consequences for the secondary electron emission, *J. Vac. Sci. Technol. A* 41 (2023) 043412].

Table 1. Composition (in at.%), maximum SEY and the Tauc gap of the a-C thin films **Error! Reference source not found..**

Sample	p_{D_2} (Pa)	C (%)	H (%)	D (%)	O (%)	SEY _{max}	E_T (eV)	ρ (g/cm ³)
Reference	0	83.4	11.7	0	4.9	0.99	0.12	1.44
0.2D	$3.8 \cdot 10^{-3}$	77.9	9.8	9.6	2.7	1.03	0.37	1.99
0.5D	$1.1 \cdot 10^{-2}$	67.8	6.0	23.7	2.5	1.15	0.78	1.91
1D	$2.6 \cdot 10^{-2}$	52.2	6.3	39.9	1.6	1.38	1.17	2.34
10D	$2.2 \cdot 10^{-1}$	45.2	2.8	50.4	1.6	2.03	2.29	1.15

From the mass densities and the Tauc gaps of the films we can already make a first estimation of their structure using general guidelines summarized in [L. Zhang, X. Wei, F. Wang, A ternary phase diagram for amorphous carbon, Carbon 94 (2015) 202-213] and by considering that deuterated carbon films are generally somewhat denser than the equivalent hydrogenated ones. It appears that the reference, 0.2D and 0.5D samples, with their Tauc gaps clearly lower than 1 eV, are most probably dominated by graphitic and partially deuterated graphite-like (a-C:D) regions. The sample 1D with E_T of 1.38 eV, high density, and large H+D content, might be closest to diamond-like a-C:D. Finally, the sample 10D, characterised by a low density and $E_T > 2$ eV, could be a typical example of polymer-like a-C:D.

3.2. XPS Measurements

Apart from carbon, the survey XPS spectra of all samples show the presence of oxygen at the surface, estimated to be about 8 at.% in all cases. The samples were not charging during the measurements apart from the sample 10D, which was measured utilising an electron flood gun for charge compensation. The O 1s line in the first four samples was situated at 532.6 eV. Assuming that the O 1s line position is the same in the sample 10D, the latter was used as a binding energy reference for that sample.

Hydrogenated/deuterated a-C is expected to be a mixture of graphitic (pure sp^2 hybridised) carbon, diamond-like carbon and different hydrocarbons in which carbon could be both in sp^2 and sp^3 hybridisation. Resolving these distributions in the C 1s photoelectron line is a complex problem due to their quite small chemical peak shifts, as extensively discussed in the literature [S. Kaciulis, Spectroscopy of carbon: from diamond to nitride films, Surf. Interface Anal. 44 (2012) 1155-1161-M.C. Biesinger, Accessing the robustness of adventitious carbon for charge referencing (correction) purposes in XPS analysis: Insights from a multi-user facility data review, Appl. Surf. Sci. 597 (2022) 153681]. The graphitic contribution is located at 284.3-284.5 eV, while a pure sp^3 C contribution is usually encountered at about 285.2 eV [P. Mérel, M. Tabbal, M. Chaker, S. Moisa, J. Morgot, Direct evaluation of the sp^3 content in diamond-like-carbon films by XPS, Appl. Surf. Sci. 136 (1998) 105-110]. The latter feature overlaps with different hydrocarbon contributions, around 285.0 eV, while at higher binding energies, further contributions related to various carbon bonds with O can be expected [M.C. Biesinger, Accessing the robustness of adventitious carbon for charge referencing (correction) purposes in XPS analysis: Insights from a multi-user facility data review, Appl. Surf. Sci. 597 (2022) 153681, G. Beamson, D. Briggs, High Resolution XPS of Organic Polymers - The Scienta ESCA300 Database, Wiley Interscience, 1992]. All peaks should be symmetric apart the one from the pure graphitic contribution, which is highly asymmetric [D.J. Morgan, Comments on the XPS analysis of carbon materials, C 7 (2021) 51, M.C. Biesinger, Accessing the robustness of adventitious carbon for charge referencing (correction) purposes in XPS analysis: Insights from a multi-user facility data review, Appl. Surf. Sci. 597 (2022) 153681]. The peak model for the graphitic contribution could be established by measuring the C 1s photoelectron line of the freshly cleaved Highly Oriented Pyrolytic Graphite (HOPG). Unfortunately, the asymmetry of the graphitic contribution is becoming less pronounced with the reduction of the cluster size and with the increase of the amount of defects in this phase. All this makes bond identification from the C 1s line fitting a challenging task without a straightforward solution. However, the elemental O concentration can be used as an additional constraint, which the carbon-oxygen bond contributions in the C 1s line need to follow. This approach, applied for all samples, except for the 10D (see below), strengthens the reliability of the interpretation of the spectra taken from the a-C coatings.

High resolution spectra of the C 1s photoelectron line of a freshly cleaved HOPG and the five samples considered in this study, together with the corresponding fittings, are presented in Figure 1.

In all cases the background was calculated using the Shirley algorithm. As in [H. M. Fernández, M. Himmerlich, P. Costa Pinto, J. Coroa, D. Sousa, A. Baris, M. Taborelli, The impact of H₂ and N₂ on the material properties and secondary electron yield of sputtered amorphous carbon films for anti-multipacting applications, *Appl. Surf. Sci.* 542 (2021) 148552], we again observe that the C 1s line becomes more symmetric with the increase of the D content in the films. One possible explanation of this trend is that the relative amount of graphitic C is being reduced and/or that the clusters are getting smaller with the increase of the D content.

The C 1s spectrum of HOPG (Figure 1a) was fitted using three contributions. The main peak (graphite), at 284.45 eV has asymmetric profile with a nomenclature LA(1.2, 2.5, 5) in CasaXPS software [N. Fairley, A. Carrick, *The Casa Cookbook – Part 1: Recipes for XPS data processing*, Acolyte Science, Cheshire, 2005] and full width at half maximum (FWHM) of 0.34 eV. It should be stressed that the same peak profile was used by M. Biesinger, failing to secure perfect agreement with the measured spectrum [M.C. Biesinger, Accessing the robustness of adventitious carbon for charge referencing (correction) purposes in XPS analysis: Insights from a multi-user facility data review, *Appl. Surf. Sci.* 597 (2022) 153681]. Since a similar problem appeared in our spectra, we introduced the second peak (graphite sat), with the same profile and a FWHM of 1.3 eV. This peak is shifted with respect to the first towards higher binding energies by 1.47 eV, while their intensity ratio is 0.106. Finally, there is a well-known wide symmetric peak at about 291.2 eV attributed to the π - π^* satellite always present in spectra of pure graphite [D.J. Morgan, Comments on the XPS analysis of carbon materials, *C* 7 (2021) 51, M.C. Biesinger, Accessing the robustness of adventitious carbon for charge referencing (correction) purposes in XPS analysis: Insights from a multi-user facility data review, *Appl. Surf. Sci.* 597 (2022) 153681].

It might be tempting to interpret the peak graphite sat as evidence of defects, such as sp³ carbon or C-H bonds. However, one should have in mind that such contributions would be symmetric. The asymmetry of this contribution would then imply non-negligible presence of other contaminants (typically O). Knowing that XPS is distinctively more sensitive to such contaminants than to C [J.H. Scofield, Hartree-Slater subshell photoionisation cross-sections at 1254 and 1487 eV, *J. Elec. Spec. Rel. Phenom.* 8 (1976) 129-137], the corresponding photoelectron lines would be clearly observable. Since this is not the case, we assume that both contributions originate from perfect graphite. They are introduced to better describe the shape of the C 1s line of HOPG, without attributing any physical interpretation to this separation. In our fittings of the graphitic contribution, we fixed the relative positions of the first two peaks and kept their intensity ratio approximately constant (see below). The intensity of the third peak was considered to be a free parameter (the latter is affected by the electronic structure and size of the graphitic clusters). The profile of all symmetric peaks (attributed to less conductive phases in a-C films) was of pseudo-Voigt type GL(30). They are attributed to sp³ carbon and C-H(D) bonds with both sp² and sp³ carbon (284.8-285.2 eV), C-O (\approx 286.6 eV), C=O (287.8-288.2 eV) and O-C=O (\approx 289.0 eV) bonds [P. Mérel, M. Tabbal, M. Chaker, S. Moisa, J. Morgot, Direct evaluation of the sp³ content in diamond-like-carbon films by XPS, *Appl. Surf. Sci.* 136 (1998) 105-110, G. Beamson, D. Briggs, *High Resolution XPS of Organic Polymers - The Scienta ESCA300 Database*, Wiley Interscience, 1992]. All symmetric peaks within one spectrum have FWHM fixed to the same value.

The essential element of the fitting procedure was to maintain the carbon-oxygen bonds of C 1s in accordance with the O:C ratio obtained from the quantitative analysis, being $8\pm 0.8\%$ for all samples. In this approach we consider that the C:O stoichiometric ratio is 1:1 for the C-O and C=O contributions and 2:1 for the COO contribution. Consistency between the composition and the C 1s fitting could only be achieved by successively decreasing the asymmetry of the graphitic line as the H+D amount increases. The degree of asymmetry is characterised here by the ratio of the parameters α and β of the line shape LA(α, β, m), which determine the spread of the tail on the high and low binding energy side, respectively (α/β being below 1 for asymmetric line shapes). In addition, final asymmetry tuning of the graphitic contribution was performed by slight modification of the intensity ratio between the main peak and the graphite sat in the range 0.078 – 0.106. This peak fitting model did not provide consistent results only for the sample 10D, as can be seen in Table 2 where the XPS fitting results are summarised. For this sample, the oxygen content is overestimated, most probably due to the charging problems that affected the shape of the C 1s line.

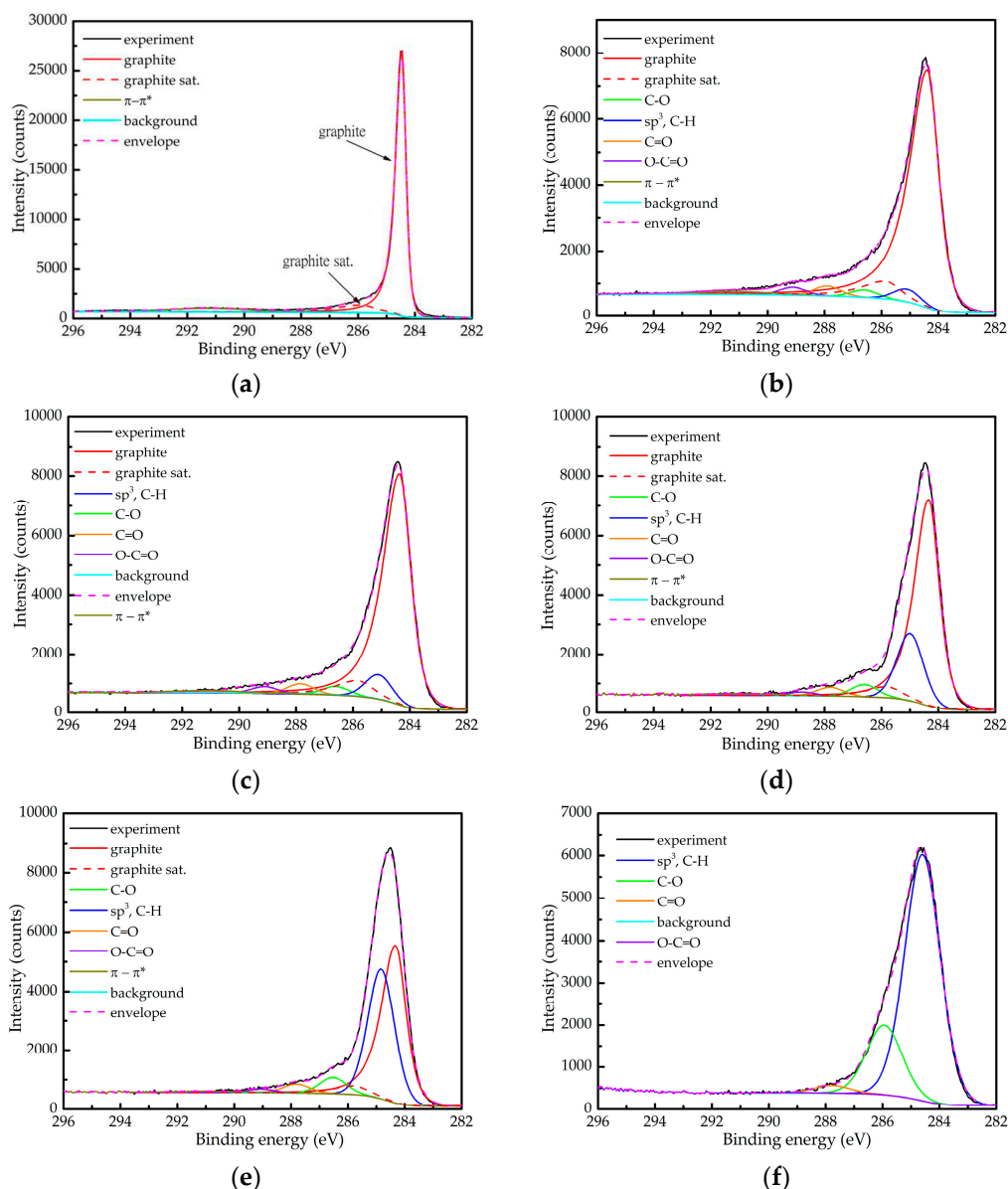


Figure 1. High resolution spectra of the C 1s state of (a) freshly cleaved HOPG, (b) reference a-C sample, (c) sample 0.2D, (d) sample 0.5D, (e) sample 1D and (f) sample 10D, and the corresponding fittings.

Fitting results of the C 1s line taken from the 5 samples and the relative content of hydrogen and deuterium taken from Table 1 are summarized in Table 2. The following general trends with the increase of the H+D relative content appear:

- The relative contribution of the graphitic component decreases and even disappears in the sample 10D;
- The relative contribution attributed to the sp^3 carbon and the hydrocarbons increases;
- The asymmetry of the graphitic component becomes less pronounced.

Therefore, increasing the amount of incorporated H/D in the films is accompanied by the higher content of hydrocarbons and reduction of the graphitic content. Besides, the graphitic regions are becoming smaller and/or with higher defect concentration.

At this point, total disappearance of the graphitic content in the sample 10D is not certain. We can only claim that there is no need to introduce the asymmetric graphitic component to obtain a good fit of the spectrum presented in Figure 1f. Since the sample 10D was charging, one could expect a deformation of the line shape. Moreover, the latter certainly took place since it was not possible to perform a good fit that would justify the correct content of the oxygen amount. While one cannot

reliably exclude the presence of some graphitic regions in that sample, their relative amount most probably does not exceed $\approx 10\%$.

Table 2. Summary of the C 1s line fittings and the relative H+D contents.

Sample	α/β	graphitic (%)	sp ³ C-H (%)	C-O (%)	C=O (%)	-(C=O)-O- (%)	H+D content (%)
reference	0.45	88.14	3.29	1.91	2.55	2.01	11.7
0.2D	0.50	85.17	6.43	2.41	2.57	1.73	19.4
0.5D	0.58	71.09	20.4	3.75	2.46	1.05	29.7
1D	0.58	52.75	38.11	4.83	2.46	0.96	46.2
10D	1.00	0	75.99	21.53	2.35	0.13	53.2

3.3. UPS Measurements

In Figure 2 we present UPS spectra close to the Fermi level (binding energy of 0 eV) taken from the reference 0.2D, 0.5D and 1D samples, as well as of the freshly cleaved HOPG. The spectra are normalised with respect to their intensities at 2 eV. The same structure cannot be reliably taken from the sample 10D due to the charging problems.

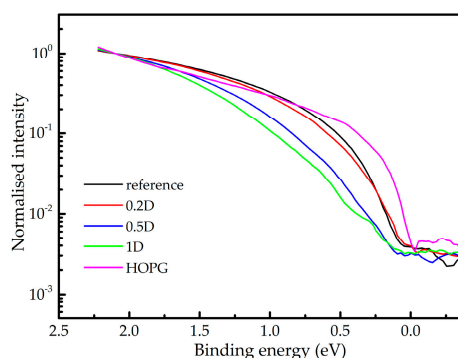


Figure 2. Valence bands of HOPG and produced a-C coatings normalised to their values at binding energy of 2 eV.

The very top of the valence band of HOPG (binding energy range 0-1 eV) can be attributed to π electrons from the K point of the Brillouin zone [A. Law, M. Johnson, and H. Hughes, Synchrotron-radiation-excited angle-resolved photoemission from single-crystal graphite, Phys. Rev. B 34 (1986) 4289]. Since the diamond-like and hydrocarbon regions have energy gaps well above 2 eV [J. Robertson, Diamond-like amorphous carbon, Mat. Sci. & Engineering R 37 (2002) 129-281], the presence of the signal in other samples is additional evidence of the graphitic regions in the a-C samples. The intensity of this structure gradually decreases with the H+D content, just as previously concluded from the XPS spectra. Closer inspection of the spectra reveals that the top of the valence band is shifting towards higher binding energy with the H+D content, verifying opening of the local energy gap attributed to the graphitic regions. The gap opening implies size reduction of the graphitic regions [A.C. Ferrari, J. Robertson, Interpretation of Raman spectra of disordered and amorphous carbon, Phys. Rev. B, 61 (2000) 14095, I. Ozfidan, M. Karkusinski, P. Hawrylak, Electronic properties and electron-electron interactions in graphene quantum dots, Phys. Status Solidi RRL 10 (2016) 13-23].

The difference between the top of the valence band and the Fermi level (the latter corresponds to the 0 eV binding energy) in the spectra presented in Figure 2 is in the range 0.0-0.2 eV. Assuming that the Fermi level is around mid-gap position, the energy gap of the graphitic regions can be roughly estimated to be ≈ 0.2 eV for the reference and 0.2D samples, and ≈ 0.4 eV for the samples 0.5D and 1D. In a first approximation, the UPS value for the reference sample corresponds to its Tauc gap (Table 1), while the mismatches between the UPS and Tauc values for the other samples (particularly for 1D) are much higher. The latter is due to the character of the Tauc gap, which corresponds to the

electronic properties of dominant components in the film, whereas UPS detects the highest occupied states. Therefore, reasonable agreement between the Tauc gap measurements and the UPS results of the reference and 0.2D samples is additional evidence of their graphitic character. On the other hand, the mismatch in the case of the other two samples confirms a lower graphitic content as already revealed by XPS.

3.4. Raman Spectroscopy

Further insight into the structure of the thin films was obtained from Raman scattering spectroscopy. Results of the Raman spectroscopy performed on the samples deposited on silicon using the 532 nm laser beam are summarised in Figure 3. The representative spectra of each sample (apart from the sample 10D) are presented in Figure 3a. The steady increase of the Raman signal with the D₂ content in the discharge gas is most probably due to the drop of the optical absorption [C.F. Adame, E. Alves, N.P. Barradas, P. Costa Pinto, Y. Delaup, I.M.M. Ferreira, H. Neupert, M. Himmerlich, S. Pfeiffer, M. Rimoldi, M. Taborelli, O.M.N.D. Teodoro, N. Bundaleski, Amorphous carbon thin films: mechanisms of hydrogen incorporation during magnetron sputtering and consequences for the secondary electron emission, *J. Vac. Sci. Technol. A* 41 (2023) 043412], which is also manifested in the increase of the Tauc gap (cf. Table 1), combined with the monotonic increase of the film thickness with the H+D content.

A feature in the range 1100-1700 cm⁻¹ corresponds to the overlapping G and D bands, being typical for various carbon phases [A.C. Ferrari, J. Robertson, Raman spectroscopy of amorphous, nanostructured, diamond-like carbon, and nanodiamond, *Phil. Trans. R. Soc. London A* 362 (2004) 2477-2512] (including deuterated a-C films [M.E.H. Maia da Costa, F.L. Freire Jr., Deuterated amorphous carbon films: Film growth and properties, *Surf. Coat. Technol.* 204 (2010) 1993-1996]). The G band is attributed to sp² carbon atoms (it is not restricted to sixfold carbon rings in graphite nor to pure carbon phases). The D band is a fingerprint of isolated sixfold carbon aromatic rings, being forbidden in a perfect graphite [A.C. Ferrari, J. Robertson, Interpretation of Raman spectra of disordered and amorphous carbon, *Phys. Rev. B*, 61 (2000) 14095]. Co-existence of both bands therefore implies presence of graphitic regions separated by disordered phases.

Apart from the G and D bands, an intense wide structure at about 2800 cm⁻¹ can be also observed in Figure 3a. Its intensity relative to the G and D bands increases with the amount of deuterium incorporated in the samples. In the sample 10D, the intensity of this structure is about 10 times greater than in the other samples measured under the same conditions, thus hindering eventual identification of the graphitic carbon (more details on this matter are provided in the Supplementary Information S1). Raman spectra of carbon-based materials may have some bands in this range. For instance, graphene is characterised by the 2D mode at around 2700 cm⁻¹ and a second order D+D' band at around 2900 cm⁻¹ [A.C. Ferrari, D.M. Basko, Raman spectroscopy as a versatile tool for studying the properties of graphene, *Nature Nanotechnology* 8 (2013) 235-246]; Raman spectra taken from polymeric amorphous carbon have in this range a C-H stretching band [A.C. Ferrari, J. Robertson, Raman spectroscopy of amorphous, nanostructured, diamond-like carbon, and nanodiamond, *Phil. Trans. R. Soc. London A* 362 (2004) 2477-2512, S. Nakahara, S. Stauss, H. Miyazoe, T. Shizuno, M. Suzuki, H. Kataoka, T. Sasaki, K. Terashima, Pulsed Laser Ablation Synthesis of Diamond Molecules in Supercritical Fluids, *App. Phys. Express* 2 (2010) 096201]. To clarify the origin of this band, Raman measurements were also performed with a He-Ne laser (wavelength of about 632.8 nm) resulting in the lack of this structure (cf. Supplementary information S1). The absolute energy position of this feature is ≈1.97 eV, corresponding well to the position of the broad emission band (1.9-2.5 eV) observed in a photoluminescence of hydrogenated a-C [Rusli and J. Robertson, G.A.J. Amarantunga, Photoluminescence behavior of hydrogenated amorphous carbon, *J. Appl. Phys.* 80 (1996) 2998-3003]. Therefore, we conclude that this feature is not a Raman signal but evidence of photoluminescence i.e. it is related to the excitation of electronic states. The latter also explains why this feature increases with the amount of incorporated deuterium in the sample.

Fitting of the Raman spectra is demonstrated in Figure 3b on the example of the sample 1D, while other fitting details can be found in the Supplementary Information S1. The spectra were fitted using 4 Lorentzian peaks after removing a linear background. Although this approach did not provide a perfect fit out of the range of interest (the latter being 1100-3000 cm⁻¹), it allows extraction of the most valuable information characterising the a-C samples. Two of the Lorentzians are readily attributed to the G and D bands at about 1550 cm⁻¹ and 1360 cm⁻¹, respectively. The peak widths and the position of the D band do not change significantly among the studied samples. There is, however, a substantial difference between the relative peak intensities from different samples as well as a

clearly pronounced shift of the G band. The wide hump related to the photoluminescence (PL), was fitted by two contributions, at about 2800 and 2150 cm^{-1} . The latter one could also be, at least partially, attributed to the CD_x stretching band [A.C. Ferrari, J. Robertson, Raman spectroscopy of amorphous, nanostructured, diamond-like carbon, and nanodiamond, *Phil. Trans. R. Soc. London A* 362 (2004) 2477-2512] (PL2/C-D). The measurements performed with 632.8 nm support this interpretation (cf. Supplementary Information S1).

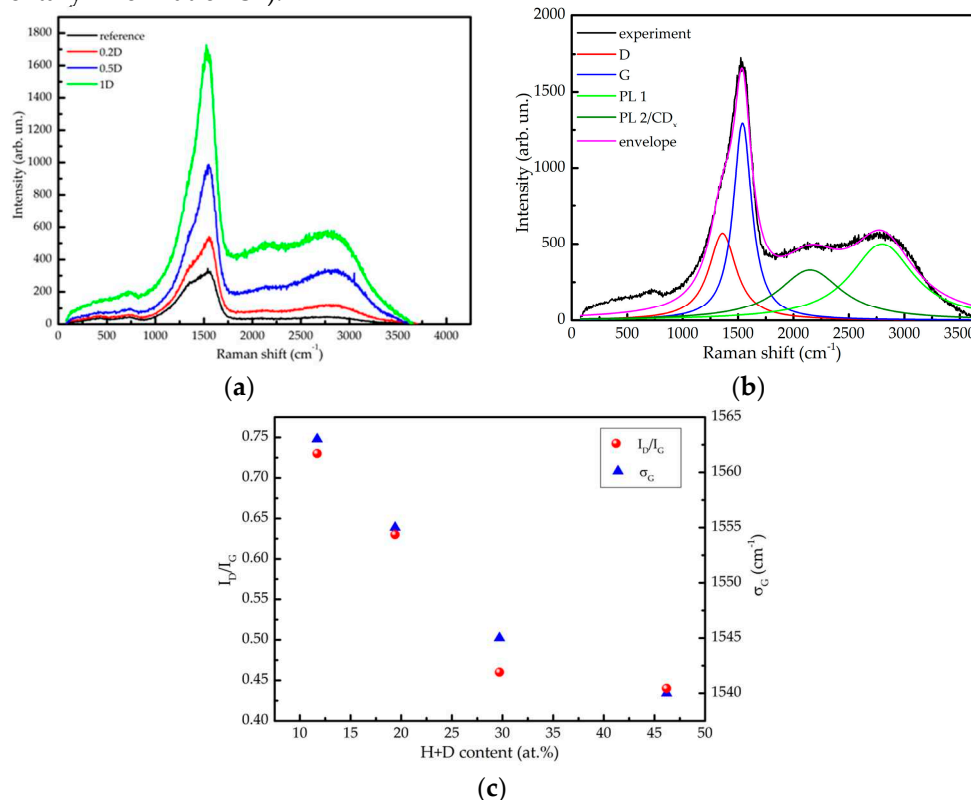


Figure 3. (a) Raman spectra of the reference, 0.2D, 0.5D and 1D samples deposited on Si substrate measured by 0.7 W 532 nm laser beam; (b) Fitting illustration on the example of the sample 1D; (c) intensity ratio of the D and G bands I_D/I_G and position of the G band maximum σ_D vs. the relative H+D film content.

Most of the findings concerning different a-C systems extracted from Raman spectra are related with the G and D bands. These bands have a large width ($\approx 200 \text{ cm}^{-1}$) in all samples, being a characteristic of disordered systems [A. Merlen, J.G. Buijnsters, C. Pardanaud, A Guide to and Review of the Use of Multiwavelength Raman Spectroscopy for Characterizing Defective Aromatic Carbon Solids: from Graphene to Amorphous Carbons, *Coatings* 7 (2017) 153]. The ratio of the intensities of the D and G bands, I_D/I_G , and the position of the G band are plotted as a function of the relative H+D content (Figure 3c). The increase of the H+D content in the films reduces the I_D/I_G intensity ratio from 0.75 to 0.45 (a similar trend has been reported in [C. Pardanaud, C. Martin, P. Roubin, G. Giacometti, C. Hopf, T. Schwarz-Selinger, W. Jacob, Raman spectroscopy investigation of the H content of heated hard amorphous layers, *Diam. Relat. Mat.* 34 (2013) 100-104] due to the increase of the hydrogen content), while the G band position σ_D is shifted from 1563 to 1540 cm^{-1} . While the observed trends are ambiguous when considered separately, a unique interpretation of this joint information is that the increase of the deuterium content corresponds to stage two of the well-known amorphisation trajectory of graphite as proposed by Ferrari and Robertson [A.C. Ferrari, J. Robertson, Interpretation of Raman spectra of disordered and amorphous carbon, *Phys. Rev. B*, 61 (2000) 14095]: transformation of nano-graphite into amorphous carbon. In this amorphisation stage, the ratio I_D/I_G is directly proportional to the average number of carbon atoms in the graphitic clusters i.e. to the square root of their diameter.

The fitting approach shown in Figure 3b was not applicable to the sample 10D due to the intense curvilinear background, mostly caused by the intense photoluminescence signal, which makes the extraction of signal in the range of the D and G bands unreliable. Nevertheless, such an attempt has been made by removing the background of a polynomial form, which resulted in an asymmetric

structure that could be mainly interpreted as the G band, while the D band is apparently lacking. Although of a limited reliability, this result implies that the graphitic phase in the sample 10D is extremely small or even absent (see above). Details concerning the analysis of the Raman spectra taken from the sample 10D can be found in the Supplementary information S1.

In addition, an attempt was made to identify the character of C-D bonds using other vibrational spectroscopies, namely FTIR and HREELS. These results are presented in the supplementary material S2 and the appendix A, respectively. In the case of FTIR, the signal attributed to C-D bonds was identified only in the case of the sample 10D, revealing that about 60% of deuterium atoms is bonded to sp^2 carbon. A similar conclusion was obtained from the measurement of the sample 1D by HREELS, confirming that the character of C-D bonds, being practically the same, is not responsible for the large difference between the electronic structures of the two samples.

4. Discussion

The XPS results and the mismatch between the Tauc plot measurements and UPS spectra evidence that the samples are generally non-uniform. Hence, the films should be considered as mixtures of different carbon phases (being a frequent situation [A.C. Ferrari, J. Robertson, Interpretation of Raman spectra of disordered and amorphous carbon, Phys. Rev. B, 61 (2000) 14095]), each characterised with their own local energy gaps. The steady increase of the films' density with the amount of incorporated deuterium up to the sample 1D can be understood as the increase of the sp^3 phases (cf. Table 1). At the same time the sample with the lowest density is 10D, despite the similar relative composition with that of 1D, clearly indicating formation of a polymeric phase [L. Zhang, X. Wei, F. Wang, A ternary phase diagram for amorphous carbon, Carbon 94 (2015) 202-213]. These estimations are fully supported by the results of the XPS, UPS and Raman analyses, revealing that increase of the deuterium content is accompanied by a decrease of the overall relative amount of the graphitic regions and their size reduction (i.e., transition from nanocrystalline graphitic phase into amorphous carbon). This is particularly evident when comparing the samples 1D and 10D, characterized with the similar relative content of deuterium (Table 1) and practically the same character of the C-D bonds. The abrupt increase of the SEY and the Tauc gap from sample 1D to 10D can be only explained by the dramatic diminishing of the graphitic component (Table 1).

A similar conclusion has been obtained by Robertson [J. Robertson, Diamond-like amorphous carbon, Mat. Sci. & Engineering R 37 (2002) 129-281], demonstrating a nearly linear dependence of the Tauc gap with the sp^2 fraction c_{sp^2} for its relative contents below 80%, practically independent from the hydrogen relative amount. Since the data presented in [J. Robertson, Diamond-like amorphous carbon, Mat. Sci. & Engineering R 37 (2002) 129-281] are compiled from the works of different authors and measured on various a-C and a-C:H samples, the points are rather scattered. Nevertheless, the line $E_T = 3 - 2.5 \cdot c_{sp^2}$ represents well the observed trend with the Tauc gap uncertainty bar of about $\Delta E_T = \pm 0.25$ eV [J. Robertson, Photoluminescence Mechanism in amorphous hydrogenated carbon, Diamond and Related Materials 5 (1996) 457-460]. The dependence of the Tauc gap and the SEY_{max} vs. the graphitic content, obtained from the XPS measurements, is shown in Figure 4. It can be observed that both E_T and SEY_{max} also decrease with the relative amount of graphitic regions. Moreover, the trend of the Tauc plot fits well with that of Robertson, presented by a dashed blue line, for the graphitic contents below 70%. The systematic shift between the two trends, which is within the uncertainty ΔE_T , can be explained by different means of measuring the graphitic content in [J. Robertson, Photoluminescence Mechanism in amorphous hydrogenated carbon, Diamond and Related Materials 5 (1996) 457-460] (using electron energy loss spectroscopy and nuclear magnetic resonance). Besides, at $c_{sp^2} > 70\%$ we observe faster drop of E_T , as expected having the non-existent band gap of graphite. These agreements imply that the methodology used to extract the graphitic fraction from the XPS spectra is quite reliable and can be also used to correlate the SEY with the graphitic content.

The decrease of the SEY with the increase of the graphitic content (observed in Figure 4) is in accordance with the expectations: higher the fraction of the sp^2 phase, lower the SEY. A simple model, based on the same assumptions as those used to derive the well-known semi-empirical equation for SEY [R.G. Lye, A.J. Dekker, Theory of Secondary Emission, Phys. Rev. 107 (1957) 977-981], was developed to support the observed experimental dependence. This equation, originally derived for uniform samples, was recently modified to encompass multilayer systems [Y. He, T. Shen, Q. Wang, G. Miao, C. Bai, B. Yu, J. Yang, G. Feng, T. Hu, X. Wang, W. Cui, Effect of atmospheric exposure on secondary electron yield

of inert metal and its potential impact on the threshold of multipactor effect, Appl. Surf. Sci. 520 (2020) 146320]. The latter approach was used as a starting point to model non-uniform a-C films as mixtures of two different phases: a graphitic one, and a polymeric one. Therefore, the polymeric phase is considered as a representative of all non-graphitic phases in the films.

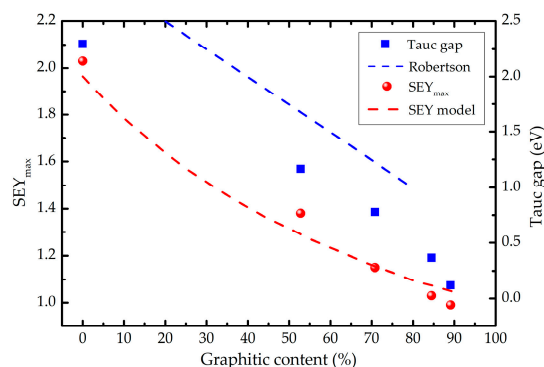


Figure 4. Dependences of the Tauc gap and the SEYmax vs. the graphitic content. The dashed blue line represents the linear dependence of the Tauc gap estimated by Robertson [J. Robertson, Photoluminescence Mechanism in amorphous hydrogenated carbon, Diamond and Related Materials 5 (1996) 457-460]. The dashed red line is the prediction of the modified semi-empirical model for the SEY developed in this work.

In the frame of the semi-empirical theory, the number of internal secondary electrons generated in a depth range ($z, z+dz$) is equal to $S(z) \cdot dz / \varepsilon(z)$, where S and ε represent the stopping power of the primary electrons and the effective energy required to create one internal secondary electron, respectively. The secondary electrons created at depth z will be then emitted with a probability equal to $0.5 \cdot \exp(-z/\lambda)$ [Y. Lin, D.C. Joy, A new examination of secondary electron yield data, Surf. Interface Anal. 37 (2005) 895–900], where λ is the mean escape depth of secondary electrons, taken from the literature [S. Ono, K. Kanaya, The energy dependence of secondary emission based on the range-energy retardation power formula, J. Phys. D: Appl. Phys. 12 (1979) 619]. Since S , λ and ε are material dependent, they will be changing from point to point of the sample interior.

The first step is to determine the parameters that characterize the electron emission properties of the graphitic and polymeric regions. For that purpose, the SEY dependencies on the primary electron energy of the reference sample and the sample 10D [C.F. Adame, E. Alves, N.P. Barradas, P. Costa Pinto, Y. Delaup, I.M.M. Ferreira, H. Neupert, M. Himmerlich, S. Pfeiffer, M. Rimoldi, M. Taborrelli, O.M.N.D. Teodoro, N. Bundaleski, Amorphous carbon thin films: mechanisms of hydrogen incorporation during magnetron sputtering and consequences for the secondary electron emission, J. Vac. Sci. Technol. A 41 (2023) 043412] were used as representatives of pure graphitic and pure polymeric material, respectively. Then, for a defined relative graphitic content, it is possible to estimate the range of primary electrons R . The samples were then modelled as a multilayer system with predefined graphitic content. However, the depth distribution of different phases within each sample is unknown. Another difficulty in establishing this distribution is in the lateral non-uniformity of the samples. To overcome this problem, a set of M depth distributions were generated (here designated as configurations), each containing the same amount of graphitic carbon, using a Monte Carlo approach. Finally, for each of the configuration, the $SEY(E)$ was calculated by generating $S(E,z) \cdot dz / \varepsilon(z)$ electrons at all depths z in the range $[0, R]$, and calculating their escape probabilities affected by the multilayer structure in the range $[0, z]$. The whole procedure is detailed in the Appendix B.

The result of the SEY model, obtained using $M = 1000$ configurations and for the primary electron energies in the range 50-1000 eV is presented in Fig. 4. Having in mind the simplifications introduced in the frame of the model, and that the calculated SEY curves were obtained without any adjustments to the existing experimental data, the agreement with the measured values is very good. There is also a built-in systematic error in the model due to the consideration that the reference sample would be purely graphitic, while its actual graphitic content is only 90%. This approximation is responsible for an overestimation of the SEY for the highest graphitic contents. Although the effective energy ε is indeed smaller in the polymeric (40.8 eV) than in the graphitic (60.4 eV) regions, the major difference between the characteristics of the two regions is the mean escape depth λ , being more than two times

smaller in graphite (4.9 nm) than in polymers (11 nm). That is probably the reason why the theoretical $SEY_{max}(sp^2 \text{ content})$ dependence can be described by an exponential decay function.

In a sample with sufficiently high content of the graphitic phase, the regions with large energy gap (e.g., diamond-like or hydrocarbon regions) will not contribute to the Tauc gap: photons that may penetrate large energy gap regions will be most likely absorbed once they enter a sufficiently large graphitic region. The reduction of the amount and size of the graphitic phase increases the optical transparency of the films and, consequently, the Tauc gap. A similar effect takes place during the transport of secondary electrons through the samples. The escape depth of internal secondary electrons, which is directly related with their energy loss mechanisms, is strongly affected by the electronic structure of a material. The efficient energy loss is secured by sufficiently long trajectories of the secondary electrons through graphitic regions characterised by very narrow energy gap. As in the case of light transmission, the graphitic phase serves as energy absorber. The increase of the graphitic content directly reduces the escape depth of internal secondary electrons and, therefore, the secondary electron yield.

Although the presence of hydrogen and deuterium in the thin films is not directly responsible for the SEY increase, it plays a key role in reducing the graphitic amount. Indeed, the H/D incorporation will naturally reduce the relative contents of both graphitic and diamond-like phases in a-C:H(D). It was revealed in the previous work that the deuterium incorporation is a consequence of target poisoning, yielding in the sputtering of CD and CD₂ molecules in parallel with C atoms [C.F. Adame, E. Alves, N.P. Barradas, P. Costa Pinto, Y. Delaup, I.M.M. Ferreira, H. Neupert, M. Himmerlich, S. Pfeiffer, M. Rimoldi, M. Taborelli, O.M.N.D. Teodoro, N. Bundaleski, Amorphous carbon thin films: mechanisms of hydrogen incorporation during magnetron sputtering and consequences for the secondary electron emission, *J. Vac. Sci. Technol. A* 41 (2023) 043412]. At the same time, pure carbon phases can only be deposited by magnetron sputtering of C atoms. The relative amount of pure carbon phases is directly related with the flux ratio of C and CD_x particles leaving the target and travelling towards the substrate. In the case of the sample 10D, this ratio was very low due to the strong target poisoning, resulting in a typical polymeric film.

5. Conclusions

Amorphous carbon coatings, deliberately modified by deuterium incorporation during the magnetron sputtering deposition, were thoroughly analysed using different electron and vibrational spectroscopies. This data was combined with previous composition and optical measurements [15], to reveal the role of H/D incorporation on the change of the secondary electron emission characteristics.

Both XPS and UPS (in combination with the Tauc gap) measurements demonstrate non-uniform character of the samples, being common for a-C materials [16]. The increase of the deuterium amount in the films is accompanied with the decrease of the fraction of the graphitic component and the cluster size. We conclude that a high content of graphitic phases in the films is responsible for a low secondary electron emission, just as it is for the low Tauc gap [18]. This phase has a local energy gap approaching to 0 eV, which reduces the escape depth of electrons travelling through it and, consequently, the secondary electron yield.

The formation of pure carbon phases (graphitic or diamond like) and hydrocarbon regions are competing processes. In our experiments, the latter is the result of target contamination by D atoms formed in the plasma, followed by the physical sputtering of CD_x molecules representing building blocks of hydrocarbon phases [15]. Therefore, the flux ratio of CD_x and C particles approaching the substrate is detrimental in this case for the relative graphitic content in the films.

Supplementary Materials: The following supporting information can be downloaded at the website of this paper posted on Preprints.org.

Author Contributions: "Conceptualization, N.B. and P.C.P.; methodology, N.B. and P.C.P.; software, N.B.; validation, A.F., M.H. and M.V.; formal analysis, N.B., J.D., M.C., A.R.; investigation, C.A., J.D., M.C., A.R., N.P.B., Y.D., H.N., M.R.; writing—original draft preparation, N.B. and P.C.P.; writing—review and editing, M.H., O.T., C.A., A.R.; visualization, C.A.; supervision, M.V., I.F., E.A. All authors have read and agreed to the published version of the manuscript."

Funding: This research was funded by the Portuguese Foundation for Science and Technology (FCT) in the frame of the project CERN/FIS-TEC/0039/2019. The support of FCT via the grants UIDB/00068/2020, UIDP/00068/2020 UIDB/04565/2020, UIDP/04565/2020 and LA/P/0140/2020 is also gratefully acknowledged. A.M. F. wishes to thank Instituto Superior Técnico for the Scientific Employment contract IST-ID/131/2018.

Data Availability Statement: Not applicable.

Acknowledgments: We acknowledge Mauro Taborelli, from CERN, for discussions and suggestions during the work on the manuscript.

Conflicts of Interest: The authors declare no conflict of interest.

Appendix A. HREELS Measurements

A.1 Experimental Setup

HREELS measurements were performed in a UHV system (operating pressure in the 10^{-7} Pa range) using a LK Technologies 2000R spectrometer. Incidence and analysis angles, measured relative to the surface normal, were 60° and 30° , respectively. Such geometry secures very high surface sensitivity. The analysis of the sample 1D was performed, as the one with potentially the highest deuterium content that can be measured (it appeared that the sample 10D was charging, as explained below). The nominal primary electron energy was 3 eV (with the elastic peak Full Width at Half Maximum (FWHM) of 12 meV). The cut-off of the spectra was measured at about 3.8 eV, corresponding to the true primary electron energy. The spectra were acquired with an energy step of 0.916 meV (7.38 cm^{-1}).

A.2 Results

In a HREELS experiment, a monoenergetic electron beam interacts with the surface region in different ways exciting vibrational modes [41] and electronic states **Error! Reference source not found.** For non-specular conditions (different incident and analysis angles) the dominant excitation mechanism is via impact (short range) interactions, occurring at distances below 1 nm. In this regime, the technique is mainly sensitive to the molecular groups in the first atomic layer, providing information on both vibrational **Error! Reference source not found.** and electronic **Error! Reference source not found.** excitations.

Fig. A1 displays the spectrum taken from the sample 1D obtained in the vibrational energy loss range. The elastic peak is asymmetric due to the excitation of low energy phonons. From 600 to $\sim 2000 \text{ cm}^{-1}$ a complex, not resolvable structure exists due to IR active modes corresponding to deformation vibrations of C-D and C-H bonds as well as to the Raman modes which can also be excited in a non-specular geometry **Error! Reference source not found.** In the stretching modes region, C-D (2000 to 2450 cm^{-1} range) and C-H (2750 to 3200 cm^{-1} range) bonds are detected **Error! Reference source not found.** Even with some uncertainty of the background, each of those two structures can be fitted to two components. The first ones at 2279 and 2150 cm^{-1} can be assigned to the stretching vibrations of D bonded to sp^2 and sp^3 carbon, respectively. This result is well correlated with the similar structures observed in FTIR measurements of the sample 10D (Supplementary Information S4). Indeed, perdeuterated benzene exhibits an IR peak at 2286 cm^{-1} **Error! Reference source not found.** In addition, in our previous work dealing with selectively deuterated polystyrenes, peaks at those frequencies were also found **Error! Reference source not found.** The equivalent C-H structure can be fitted to two components at 3054 and 2938 cm^{-1} , which can be assigned to hydrogen bonds with sp^2 and sp^3 hybridised carbon, respectively. At higher energy loss (3558 cm^{-1}) another peak is detected, that we assigned to the O-H stretching in an alcohol group. The equivalent deuterated group, which should be present between the C-D and C-H structures, was not detected. One possible reason is the corresponding energy loss cross section is lower for the O-D, similarly to the C-D bonds as compared to the C-H bonds (see below). In addition, lack of this bond may imply that OH groups mainly originate from the surface contamination due to air exposure that took place after the deposition. This interpretation is supported by the facts that the vacuum system was baked prior to the deposition and had very low residual gas pressure (below $1 \cdot 10^{-8}$ Pa), and that the oxygen amount measured by XPS was higher than that obtained by IBA [15].

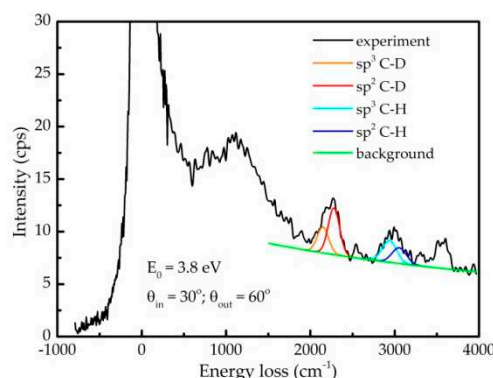


Figure A1. Vibrational HREELS spectrum taken from the sample 1D. The partial fittings of C-H and C-D stretching modes are also included.

The ratio of surface concentrations of D (n_D) and H (n_H) atoms can be estimated from the ratios of the respective peak areas A_D and A_H , and the inelastic loss cross sections attributed to the C-D (σ_D) and C-H (σ_H) bonds:

$$\frac{n_D}{n_H} = \frac{A_D}{A_H} \cdot \frac{\sigma_H}{\sigma_D} \quad (\text{A1})$$

The corresponding cross-section ratios σ_H/σ_D in IR spectroscopy are around 1.81 (aromatic bonds) and 2.17 (aliphatic bonds), while the equivalent magnitudes are somewhat lower in HREELS **Error! Reference source not found.** Having in mind experimental difficulties in calibrating HREELS in that work, we prefer to use the cross-section ratios from the IR spectroscopy in the attempt to determine the concentration ratios n_D/n_H . Since the cross-section ratios do not depend strongly on the bonding character, their average (1.99) was used, yielding $n_D/n_H = 3.0$. The same magnitude in the sample 1D is about 2 times greater when measured by IBA, most probably due to very different information depths.

In further analysis, we consider that the cross sections for H/D bonded with sp^2 and sp^3 carbon are approximately the same. If so, the peak intensity ratios obtained from the fittings directly correspond to the fractions of D and H bonded with sp^2 and sp^3 hybridized carbon atoms. By implementing this approach, it appears that about 64 % of D atoms are bonded with sp^2 carbon, while this percentage is only 42 % for H atoms. One should, however, have in mind that this ratio does not correspond directly to the relative ratios of hydrocarbon species with sp^2 and sp^3 carbon, since the relative amount of H/D in saturated aliphatic hydrocarbons is certainly higher than in compounds containing sp^2 hybridised carbon atoms.

When comparing the D:H ratio restricted to sp^2 or sp^3 carbon (using the actual intensity ratios of the corresponding cross-sections), we get the values of 4.23 and 2.03, respectively. While the ratio for the bonds with sp^2 carbon approaches the corresponding values obtained by IBA [15], the ratio for the sp^3 carbon is clearly lower. Again, as for the O-H, the results obtained can be explained by the surface contamination that took place after the deposition, which mainly consists of aliphatic saturated hydrocarbons (airborne). Namely this is the reason for the reduced n_D/n_H ratio at the surface as compared to the values measured by IBA, but also for the different ratios in the case of the sp^2 and sp^3 carbon hybridisations.

Appendix B. Modelling SEY from Non-Uniform a-Carbon Samples

B.1 Semi-Empirical Theory of Secondary Electron Emission and Its Application to Graphitic and Polymeric Samples

The semi-empirical theory of secondary electron emission are based on the following assumptions **Error! Reference source not found.**:

- all primary electrons have the same range R in a material, which can be described by the power law $R = b \cdot E^n$, with E being the energy of incident electrons, while b is the material constant;

- the number of internal secondary electrons generated in the depth interval $(z, z + \Delta z)$ is directly proportional to the stopping power of primary electrons $S(z) = -dE/dz$, $\Delta N(z) = S(z)\Delta z/\varepsilon$, where ε is the effective energy required to create one internal secondary electron;
- electron stopping power is assumed to be constant, and frequently its average value along the trajectory $E/R(E)$ is used;
- the probability that an internal secondary electron will be emitted is $0.5 \cdot \exp(-z/\lambda)$, where λ is an electron escape depth (a material dependent parameter).

Starting from these assumptions, one can easily derive the following equation for the energy dependence of SEY:

$$SEY = \frac{0.5 \cdot \lambda}{\varepsilon \cdot b} \cdot \frac{1 - e^{-\frac{b \cdot E^n}{\lambda}}}{E^{n-1}} \quad (B1)$$

After introducing the relative energy $E_r = E/E_m$, where E_m is the energy at which SEY has maximum, and a parameter $x = R(E_m)/\lambda$, the expression (B1) can be transformed into

$$SEY_r = \frac{SEY}{SEY_{max}} = \frac{1}{1 - e^{-x}} \cdot \frac{1 - e^{-x \cdot E_r^n}}{E_r^{n-1}} \quad (B2)$$

Since x is the solution of the transcendent equation $e^x = 1 + \frac{n}{n-1} \cdot x$ **Error! Reference source not found.**, the shape of the $SEY(E)$ curve is fully described by the single parameter n , which can be then obtained by fitting the experimental $SEY(E)$ curve to the eq. B2 **Error! Reference source not found.**. By combining the eqs. B1 and B2, the knowledge of n enables to calculate the energy ε as

$$\varepsilon = \frac{0.5 \cdot (1 - e^{-x}) \cdot E_m}{x \cdot SEY_{max}} \quad (B3)$$

In our approach, we consider the reference and the 10D samples as representatives of dominantly graphitic and polymeric samples, respectively. Their $SEY_r(E_r)$ curves (obtained from the $SEY(E)$ curves from **Error! Reference source not found.**), presented in Figure B1, can be well described within the semi-empirical theory using the values $n = 1.6$ (the reference) and $n = 1.5$ (10D). The corresponding parameters x were then calculated by solving the above mentioned transcendent equation, as well as the effective energies ε using the eq. B3 and the experimental values for E_m and SEY_{max} . The obtained values for the reference and 10D samples are 60.4 and 40.8 eV, respectively. The escape depths used for graphitic and organic carbon samples, taken from **Error! Reference source not found.**, are 4.9 and 11 nm, respectively. After calculating the factors b as $x \cdot \lambda / E_m^n$ (from the assumed $R(E)$ dependence and the definition of the parameter x), we were able to calculate the SEY curves in the frame of the semi-empirical theory.

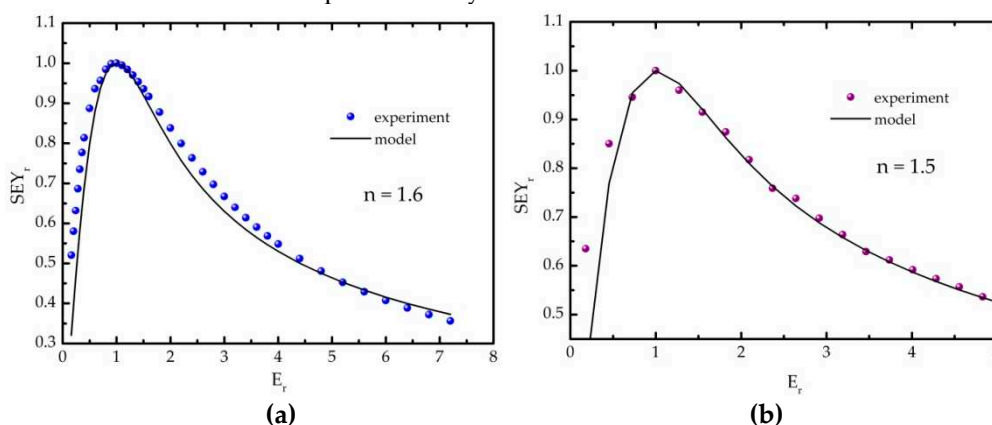


Figure B1. Determination of the parameter n in the case of the a) reference and b) 10D sample, representing dominantly graphitic and polymeric samples, respectively.

The experimental and modelled SEY curves are compared in Figure B2. Although experimental curves were used to determine some of the parameters, namely n and ε , it should be stressed that there were no adjustments of calculated values to the experimental SEY curves. With this in mind, the semi-empirical theory provides very good description of the experimental SEY curves. This is particularly valid for the reference sample (Figure B2a), for which an excellent agreements for both SEY_{max} and E_m are obtained. That is not the case with the polymeric sample,

particularly concerning the maximum position. Possible reason for such discrepancy could be in the different measurement approach for the sample 10D, which was affected by charging (see Section 2 for details). Nevertheless, even for that sample the model curve appears to be a good representative of the experimental dependence.

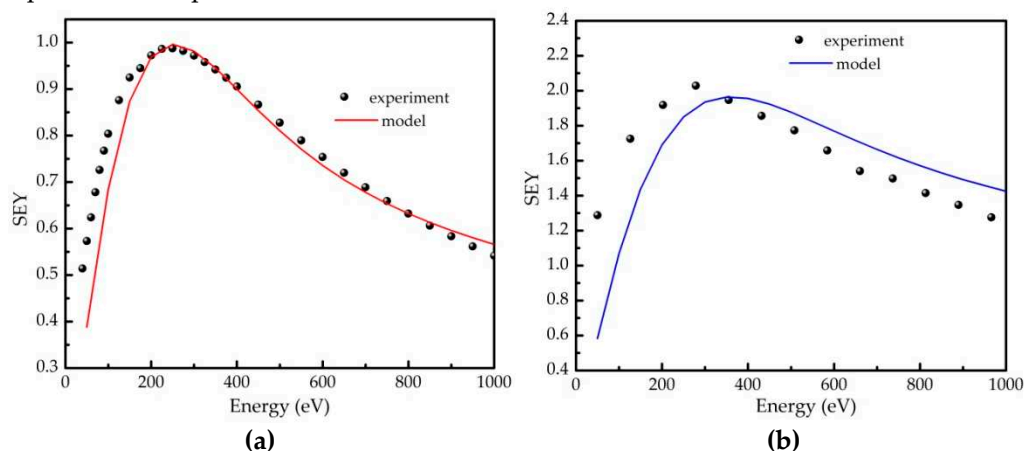


Figure B2. Comparison of the experimental and calculated SEY in the case of the a) reference and b) 10D sample.

B.2 Model Description

The semi-empirical theory, including its recent upgrade for multilayer systems **Error! Reference source not found.**, is a 1D continuous model. Therefore, a non-uniform material can be only considered as a multilayer system. For a fixed sample composition, there is a huge number of depth distributions of polymeric and graphitic layers (here designated as configurations) with very different SEY. Some of the possible configurations in the case of a sample consisting of 30% of graphitic component are presented in Figure B3. Extreme configurations, consisting of only 2 layers (one for each component), would have very different SEY, depending which phase is on the top. Since a representative configuration cannot be determined, we considered this problem in the frame of the Monte Carlo approach.

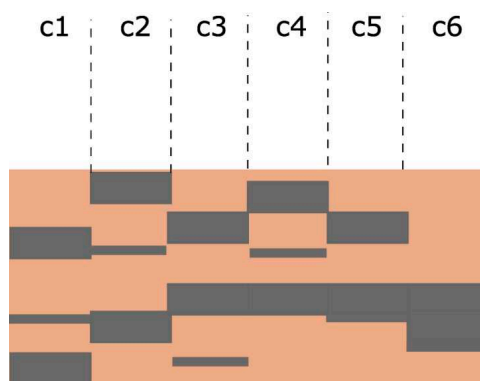


Figure B3. Illustration of different configurations ck ($k = 1, 2, \dots$), each containing the same relative amounts of graphitic (grey) and polymeric (brown) regions, which will be characterised with very different SEY curves.

The first step was to determine range of the primary electrons using the assumptions built into the semi-empirical theory: the stopping power of electrons in each region i is constant and can be determined as $S_i = E/R_i$, where R_i is the range in a uniform sample consisting of the component i . Let L_p and L_g be the total lengths of trajectories of primary electrons passing through the polymeric and graphitic regions, respectively. The range of primary electrons will then be $R = L_p + L_g$. Since all of the primary electron energy is transferred to the material after the primary electrons pass the trajectory of length R , we can write $E = S_g \cdot L_g + S_p \cdot L_p = \frac{E}{R_g} \cdot L_g + \frac{E}{R_p} \cdot L_p$, i.e. $1 = \frac{L_g}{R_g} + \frac{L_p}{R_p}$. We assume that the fraction of trajectory passing through the component i equals the relative concentration of

that component n_i i.e. $L_i/R = n_i$. In that case, the range of primary electrons through the two-component sample can be written as

$$R = \left(\frac{n_p}{R_p} + \frac{n_g}{R_g} \right)^{-1}. \quad (\text{B4})$$

The sample is considered to have thickness equal to the range R obtained for the maximum primary electron energy, calculated from the known composition, using eq. B4. The sample is divided in 100 layers of equal thickness, $\Delta z = R/100$. The composition of each layer is determined using the Monte Carlo approach, knowing that the probability that a particular layer is graphitic/polymeric equals $n_g/(1 - n_g)$. Once a configuration is formed, the SEY is calculated by creating in each layer of index i $S_i \cdot \Delta z / \varepsilon_i$ internal secondary electrons, which will leave the material with a probability $0.5 \cdot \prod_{j=1}^{i-1} e^{-\frac{\Delta z}{\lambda_j}}$ (the indices i and j increase with the layer depth). For a particular configuration, SEY is calculated for different primary electron energies. This procedure is then repeated for M different configurations characterized by the same sample composition, and the final $SEY(E)$ is obtained as an average of all curves obtained for different configurations. The results presented in the paper are obtained for $M = 1000$.

References

1. O. Gröbner, Bunch induced multipactoring, CM-P0064850, CERN Libraries, Geneva, Switzerland, presented at the 10th International Conference on High-Energy Accelerators, 11th-17th of July 1977, Serpukhov, USSR
2. R. Cimino, I.R. Collins, M.A. Furman, M. Pivi, F. Ruggiero, G. Rumolo, F. Zimmermann, Can low-energy electrons affect high-energy physics accelerators?, *Phys. Rev. Lett.* 93 (2004) 014801
3. R.A. Kishek, Y.Y. Lau, L.K. Ang, A. Valfells, R.M. Gilgenbach, Multipactor discharge on metals and dielectrics: historical review and recent theories, *Phys. Plasmas* 5 (1998) 2120–2126
4. J. Puech, et al., A multipactor threshold in waveguides: theory and experiment, in: J.L. Hirshfield, M.I. Petelin (Eds.), *Quasi-Optical Control of Intense Microwave Transmission*. NATO Science Series II: Mathematics, Physics, and Chemistry vol. 203, Springer, Dordrecht, 2006.
5. J. Hillairet, M. Goniche, N. Fil, M. Belhaj, and J. Puech, Multipactor in High Power Radio-Frequency Systems for Nuclear Fusion, presented at the International Workshop on Multipactor, Corona and Passive Intermodulation, MULCOPIM 2017, 5th-7th of April 2017 Noordwijk, The Netherlands
6. G. Skripka, G. Iadarola, L. Mether, G. Rumolo, Non-monotonic dependence of heat loads induced by electron cloud on bunch population at the LHC, *Eur. Phys. J. Plus* 137 (2022) 849
7. C. Yin Vallgren, G. Arduini, J. Bauche, S. Calatroni, P. Chiggiato, K. Cornelis, P. Costa Pinto, B. Henrist, E. Métral, H. Neupert, G. Rumolo, E. Shaposhnikova, M. Taborelli, Amorphous carbon coatings for the mitigation of electron cloud in the CERN super proton synchrotron, *Phys. Rev. ST Accel. Beams* 14 (2011) 071001
8. F. Willeke, J. Beebe-Wang, *Electron Ion Collider Conceptual Design Report 2021*. United States: N. p., 2021. Web. doi:10.2172/1765663.
9. S. Verdú-Andrés et al., A beam screen to prepare the RHIC vacuum chamber for EIC hadron beams: conceptual design and requirements, 12th International Particle Accelerator Conference - IPAC'21, May 24 - 28, 2021 Web. <https://www.osti.gov/servlets/purl/1784486>
10. R.F. Egerton, *Electron-Energy Loss Spectroscopy in the Electron Microscope 3rd edn*. Springer, New York, 2011
11. S. Ono, K. Kanaya, The energy dependence of secondary emission based on the range-energy retardation power formula, *J. Phys. D: Appl. Phys.* 12 (1979) 619
12. P. Costa Pinto, et al., Carbon coating of the SPS dipole chambers. *AIP Conf. Proc.* C 12 (August 2013) 141–148
13. A. Santos, N. Bundaleski, B.J. Shaw, A.G. Silva, O.M.N.D. Teodoro, Increase of Secondary Electron Yield of Amorphous Carbon Coatings under High Vacuum Conditions. *Vacuum* 98 (2013) 37-40
14. H. M. Fernández, M. Himmerlich, P. Costa Pinto, J. Coroa, D. Sousa, A. Baris, M. Taborelli, The impact of H2 and N2 on the material properties and secondary electron yield of sputtered amorphous carbon films for anti-multipacting applications, *Appl. Surf. Sci.* 542 (2021) 148552
15. C.F. Adame, E. Alves, N.P. Barradas, P. Costa Pinto, Y. Delaup, I.M.M. Ferreira, H. Neupert, M. Himmerlich, S. Pfeiffer, M. Rimoldi, M. Taborelli, O.M.N.D. Teodoro, N. Bundaleski, Amorphous carbon thin films: mechanisms of hydrogen incorporation during magnetron sputtering and consequences for the secondary electron emission, *J. Vac. Sci. Technol. A* 41 (2023) 043412
16. A.C. Ferrari, J. Robertson, Interpretation of Raman spectra of disordered and amorphous carbon, *Phys. Rev. B* 61 (2000) 14095

17. D. Roy, G. F. Samub, M. K. Hossain, C. Janáky, K. Rajeshwar, On the measured optical bandgap values of inorganic oxide semiconductors for solar fuels generation, *Catalysis Today* 300 (2018) 136-144
18. J. Robertson, Diamond-like amorphous carbon, *Mat. Sci. & Engineering R* 37 (2002) 129-281
19. A.C. Ferrari, J. Robertson, Interpretation of Raman spectra of disordered and amorphous carbon, *Phys. Rev. B*, 61 (2000) 14095
20. L. Zhang, X. Wei, F. Wang, A ternary phase diagram for amorphous carbon, *Carbon* 94 (2015) 202-213
21. S. Kaciulis, Spectroscopy of carbon: from diamond to nitride films, *Surf. Interface Anal.* 44 (2012) 1155-1161
22. P. Mérel, M. Tabbal, M. Chaker, S. Moisa, J. Morgot, Direct evaluation of the sp³ content in diamond-like-carbon films by XPS, *Appl. Surf. Sci.* 136 (1998) 105-110
23. D.J. Morgan, Comments on the XPS analysis of carbon materials, *C* 7 (2021) 51
24. M.C. Biesinger, Accessing the robustness of adventitious carbon for charge referencing (correction) purposes in XPS analysis: Insights from a multi-user facility data review, *Appl. Surf. Sci.* 597 (2022) 153681
25. G. Beamson, D. Briggs, *High Resolution XPS of Organic Polymers - The Scienta ESCA300 Database*, Wiley Interscience, 1992
26. N. Fairley, A. Carrick, *The Casa Cookbook – Part 1: Recipes for XPS data processing*, Acolyte Science, Cheshire, 2005
27. J.H. Scofield, Hartree-Slater subshell photoionisation cross-sections at 1254 and 1487 eV, *J. Elec. Spec. Rel. Phenom.* 8 (1976) 129-137
28. A. Law, M. Johnson, and H. Hughes, Synchrotron-radiation-excited angle-resolved photoemission from single-crystal graphite, *Phys. Rev. B* 34 (1986) 4289
29. I. Ozfidan, M. Karkusinski, P. Hawrylak, Electronic properties and electron-electron interactions in graphene quantum dots, *Phys. Status Solidi RRL* 10 (2016) 13-23
30. A.C. Ferrari, J. Robertson, Raman spectroscopy of amorphous, nanostructured, diamond-like carbon, and nanodiamond, *Phil. Trans. R. Soc. London A* 362 (2004) 2477-2512
31. M.E.H. Maia da Costa, F.L. Freire Jr., Deuterated amorphous carbon films: Film growth and properties, *Surf. Coat. Technol.* 204 (2010) 1993-1996
32. A.C. Ferrari, D.M. Basko, Raman spectroscopy as a versatile tool for studying the properties of graphene, *Nature Nanotechnology* 8 (2013) 235-246
33. S. Nakahara, S. Stauss, H. Miyazoe, T. Shizuno, M. Suzuki, H. Kataoka, T. Sasaki, K. Terashima, Pulsed Laser Ablation Synthesis of Diamond Molecules in Supercritical Fluids, *App. Phys. Express* 2 (2010) 096201
34. Rusli and J. Robertson, G.A.J. Amaratunga, Photoluminescence behavior of hydrogenated amorphous carbon, *J. Appl. Phys.* 80 (1996) 2998-3003
35. A. Merlen, J.G. Buijnsters, C. Pardanaud, A Guide to and Review of the Use of Multiwavelength Raman Spectroscopy for Characterizing Defective Aromatic Carbon Solids: from Graphene to Amorphous Carbons, *Coatings* 7 (2017) 153
36. C. Pardanaud, C. Martin, P. Roubin, G. Giacometti, C. Hopf, T. Schwarz-Selinger, W. Jacob, Raman spectroscopy investigation of the H content of heated hard amorphous layers, *Diam. Relat. Mat.* 34 (2013) 100-104
37. J. Robertson, Photoluminescence Mechanism in amorphous hydrogenated carbon, *Diamond and Related Materials* 5 (1996) 457-460
38. R.G. Lye, A.J. Dekker, Theory of Secondary Emission, *Phys. Rev.* 107 (1957) 977-981
39. Y. He, T. Shen, Q. Wang, G. Miao, C. Bai, B. Yu, J. Yang, G. Feng, T. Hu, X. Wang, W. Cui, Effect of atmospheric exposure on secondary electron yield of inert metal and its potential impact on the threshold of multipactor effect, *Appl. Surf. Sci.* 520 (2020) 146320
40. Y. Lin, D.C. Joy, A new examination of secondary electron yield data, *Surf. Interface Anal.* 37 (2005) 895–900
41. H. Ibach, D. L. Mills, *Electron Energy Loss Spectroscopy and Surface Vibrations* (Acad. Press, New York, 1982)
42. A.M. Botelho do Rego, M. Rei Vilar, J. Lopes da Silva, Mechanisms of vibrational and electronic excitations of polystyrene films in high resolution electron energy loss spectroscopy, *J. Elec. Spectr. Rel. Phenom.* 85 (1997) 81-91
43. M. Rei Vilar, A.M. Botelho do Rego, J. Lopes da Silva, F. Abel, V. Quillet, M. Schott, S. Petitjean, R. Jérôme, Quantitative Analysis of Polymer Surfaces and Films Using Elastic Recoil Detection Analysis (ERDA), Fourier Transform Infrared Spectroscopy (FTIRS), and High-Resolution Electron Energy Loss Spectroscopy (HREELS) *Macromolecules* 27 (1994) 5900-5906
44. A.M. Botelho do Rego, A.M. Ferraria, M. Rei Vilar, Grafting of Cobaltic Protoporphyrin IX on Semiconductors toward Sensing Devices: Vibrational and Electronic High-Resolution Electron Energy Loss Spectroscopy and X-ray Photoelectron Spectroscopy Study, *J. Phys. Chem. C.* 117 (2013) 22298–22306
45. A.M. Botelho do Rego, J.L. da Silva, M. Rei Vilar, R. Voltz, Resonance mechanisms in electron energy loss spectra of stearic acid Langmuir-Blodgett monolayers revealed by isotopic effects, *J. Electron. Spectrosc.* 87, (1998) 221-230.

46. M. Diem, *Modern Vibrational Spectroscopy and Micro-Spectroscopy*, 2nd edition (John Wiley&Sons Ltd, The Atrium, 2015)
47. NIST Standard Reference Database SRD Number 69. Last access to data: May 2023 DOI: <https://doi.org/10.18434/T4D303>
48. M. Rei Vilar, M. Schott, J.J. Pireaux, C. Grégoire, P.A. Thiry, R. Caudano, A. Lapp, A.M. Botelho do Rego, J. Lopes da Silva, Study of Polymer Film Surfaces by EELS Using Selectively Deuterated Polystyrene, *Surf. Sci.* 189/190, 927-934 (1987)
49. S. Clerc, J.R. Dennison, R. Hoffmann, J. Abbott, On the computation of secondary electron emission models, *IEEE Trans. Plasma Sci.* 34 (2006) 2219–2225
50. G. F. Dionne, Origin of secondary electron emission yield curve parameters, *J. Appl. Phys.* 46 (1975) 3347-3351
51. N. Bundaleski, M. Belhaj, T. Gineste, O.M.N.D. Teodoro, Calculation of the angular dependence of the total electron yield, *Vacuum* 122 (2015) 255-259

Disclaimer/Publisher's Note: The statements, opinions and data contained in all publications are solely those of the individual author(s) and contributor(s) and not of MDPI and/or the editor(s). MDPI and/or the editor(s) disclaim responsibility for any injury to people or property resulting from any ideas, methods, instructions or products referred to in the content.